

Research Article

Characterization of Pr-Doped LaF_3 Nanoparticles Synthesized by Different Variations of Coprecipitation Method

M. S. Pudovkin , D. A. Koryakovtseva, E. V. Lukinova, S. L. Korableva ,
R. Sh. Khusnutdinova, A. G. Kiiamov , A. S. Nizamutdinov, and V. V. Semashko

Kazan Federal University, Kazan, Tatarstan 420008, Russia

Correspondence should be addressed to M. S. Pudovkin; jaz7778@list.ru

Received 25 July 2018; Revised 16 October 2018; Accepted 24 December 2018; Published 7 March 2019

Academic Editor: William Yu

Copyright © 2019 M. S. Pudovkin et al. This is an open access article distributed under the Creative Commons Attribution License, which permits unrestricted use, distribution, and reproduction in any medium, provided the original work is properly cited.

A set of $\text{Pr}^{3+}:\text{LaF}_3$ nanoparticles (NPs) were synthesized via coprecipitation method at three stoichiometric proportions of $\text{La}(\text{NO}_3)_3$, $\text{Pr}(\text{NO}_3)_3$, and NaF (1:0.8, 1:1, and 1:6, respectively). Two ways of mixing of the $\text{La}(\text{NO}_3)_3$, $\text{Pr}(\text{NO}_3)_3$, and NaF solutions (dropwise and swift addition) were used. One sample was subjected to microwave (MW) treatment for 30, 90, and 180 min. All the samples were characterized by transmission electron microscopy (TEM) and X-ray diffraction (XRD). For all the samples, optical spectroscopy experiments were carried out. The XRD data were analyzed via the Debye-Scherrer and Williamson-Hall methods. It was revealed that the way of mixing of the $\text{La}(\text{NO}_3)_3$, $\text{Pr}(\text{NO}_3)_3$, and NaF solutions strongly affects the shape of the NPs. The slow dropwise addition of the NaF solution leads to the plate-like NP (PLNP) formation; otherwise, the swift addition of the NaF solution leads to the formation of more sphere-like NPs (SLNPs). The size and regularity in shape of the NP increase with the increasing stoichiometric proportion of $\text{La}(\text{NO}_3)_3$, $\text{Pr}(\text{NO}_3)_3$, and NaF from 1:0.8 to 1:6. The size and regularity in shape of the SLNPs increase with the increasing time of MW treatment. The Debye-Scherrer and Williamson-Hall methods confirmed the anisotropic shape of the PLNPs. The Williamson-Hall method showed that the values of strain are almost similar for all the samples (around 14×10^{-4}). Optical spectroscopy experiments revealed that although all the samples have an equal chemical composition, the luminescence lifetimes for different samples differ between each other. The luminescence lifetime of the PLNPs is less than that of the SLNPs having an equal stoichiometric proportion of $\text{La}(\text{NO}_3)_3$, $\text{Pr}(\text{NO}_3)_3$, and NaF. The luminescence lifetime of the 1:1 SLNPs increases with the increasing time of MW treatment.

1. Introduction

Rare-earth-doped fluoride nanomaterials hold a special role among other luminescent nanomaterials because of their excellent magnetic properties [1, 2], photostability [3, 4], long luminescent lifetimes [5], sharp emission bands [6], low toxicity [7], high melting point, and good resistance to thermal and chemical attacks [8]. These nanomaterials have a huge variety of applications including luminescent nanothermometry [9, 10] and bioimaging [11].

During the last two decades, immense progress has been done toward facile and economy methods of synthesis of LnF_3 ($\text{Ln} = \text{La}, \text{Ce}, \text{Pr}$, and others) nanoparticles (NPs) doped by rare-earth ions [12]. Among these methods of

synthesis, a coprecipitation method is considered one of the cheapest and easiest methods of synthesis of NPs [13]. On the one hand, it provides a synthesis of LnF_3 NPs with desired size, shape, and structure [14]. Usually, this method does not require toxic organic precursors as well as sophisticated and expensive laboratory equipment. On the other hand, this method has some disadvantages such as the presence of captured [15] and absorbed [8] water in NPs. These water molecules may significantly contribute into the luminescence-quenching processes [16]. Also, for some cases, NPs synthesized via such method can be characterized by relatively low crystallinity [17], presence of undesirable crystal phase, and broad size distribution and irregularity of NPs shape [18]. For this method, additional

modifications of some parameters of synthesis such as the stoichiometric ratio of fluorinating agents and rare-earth salts or/and using microwave-assisted treatment can significantly improve the quality of nanomaterials.

Microwave-assisted treatment of fluoride NPs was developed in [15, 17, 19–21]. This method has been widely applied in chemical reactions and material synthesis due to its unique reaction effects such as rapid volumetric heating and consequent dramatic increase in reaction rates [22]. In this case, the growth mechanism is likely a dissolution–recrystallization process according to the conventional hydrothermal method for preparing rare-earth fluoride NPs and hydroxide nanorods/nanotubes [23]. However, in [17], it was shown that the recrystallization process for PrF_3 and DyF_3 NPs during the microwave-assisted treatment is different and depends on such factors as difference in symmetry and difference of lattice energies for lanthanide ions Pr^{3+} and Dy^{3+} . Also, in [17], it was reported that crystallinity of DyF_3 NPs obtained via coprecipitation method was significantly improved after microwave-assisted treatment for 7 hours without considerable changing of an average size of the DyF_3 NPs. In [8], it is reported that fullerene-like PrF_3 NPs were obtained after microwave-assisted treatment of a colloidal solution of irregular-shaped PrF_3 NPs synthesized via coprecipitation method crystallinity [17], and remove captured water from the NPs core [15]. Hence, the luminescence lifetime and luminescence quantum yield will be improved without the significant complication of the synthesis procedure.

The excess of fluorinating agents is commonly used in the synthesis of fluoride NPs in order to provide a single-phased composition of NPs and regularity of size and shape. For example, the nonstoichiometric proportions of rare-earth nitrates and fluorinating agent are often used for the synthesis of hexagonal structured $\text{Yb}^{3+}/\text{Er}^{3+}:\text{NaYF}_4$ NPs. Also, it is reported in [18] that the regularity of the size and shape of $\text{Eu}^{3+}:\text{NaYF}_4$ was achieved by using the 5-fold stoichiometric proportion of NaF.

Usually, NPs synthesized via the methods mentioned above are crystalline particles. In order to determine the phase of the NPs and assess their crystallinity, the X-ray diffraction method is used. Moreover, the additional information can be extracted from X-ray data. For example, unlike the bulk crystals, the nanosized crystalline particles demonstrate broadened diffraction peaks. This peak broadening stems from crystallite size and different crystal imperfections such as lattice strains. Hence, the two main properties which can be extracted from the analysis of peak width are the crystallite size and lattice strain [24]. There are methods such as Debye-Scherrer and Williamson-Hall which enable to estimate for example lattice strains for additional characterization of different nanomaterials.

The Pr^{3+} -doped LaF_3 ($C_{\text{Pr}} = 7\%$) NPs were chosen as an object of research because of their unique properties such as thermally coupled $^3\text{P}_1$ to $^3\text{P}_0$ electron states of Pr^{3+} ions [25–27]. This property can be used in luminescent nanothermometry [12, 28]. The emission spectrum of Pr^{3+} in lanthanum fluoride host matrix overlaps with photosensitizers such as acridine ($\text{C}_{13}\text{H}_9\text{N}$) and cyanine which are highly relevant

in hybrid radiotherapy–photodynamic therapy mentioned above [3]. Hence, this system Pr^{3+} -doped LaF_3 nanoparticles can be used for different application including biology and medicine [29].

In this study, we focus on studying the physical properties of the Pr^{3+} -doped LaF_3 of different size and shape synthesized via coprecipitation method by using different ways of mixing of rare-earth salts and fluorinating agents, varying stoichiometric proportion of rare-earth salts and fluorinating agents, and performing microwave-assisted treatment for chosen samples.

In order to assess the contribution of size and shape of the NPs and also their crystallinity into the optical properties of the NPs, we characterize the obtained NPs via transmission electron microscopy (TEM), X-ray analysis, and optical spectroscopy. We also analyze X-ray data via the Debye-Scherrer and Williamson-Hall methods in order to calculate crystallite size and strains of the NPs. For a chosen sample, we studied the influence of microwave irradiation on the physical properties of the NPs. Additionally, the information concerning microstrains into the NPs extracted from the X-ray data can be very useful for understanding some physical properties of NPs.

2. Materials and Methods

2.1. Classification of the Samples. All the $\text{Pr}^{3+}:\text{LaF}_3$ ($C_{\text{Pr}} = 7\%$ (atomic)) NPs were synthesized via coprecipitation method using a chemical reaction described in [8, 15]. The obtained $\text{Pr}^{3+}:\text{LaF}_3$ ($C_{\text{Pr}} = 7\%$) samples can be divided into two groups: sphere-like NPs (SLNPs) and plate-like NPs (PLNPs). Synthesis of both SLNPs and PLNPs was carried out at 3 different stoichiometric proportions of $\text{La}(\text{NO}_3)_3$, $\text{Pr}(\text{NO}_3)_3$, and NaF (1:0.8, 1:1, and 1:6, respectively). For the sake of simplicity, we will use abbreviations 1:0.8, 1:1, and 1:6 and SLNPs or PLNPs in order to name the samples. For example, 1:6 SLNPs means sphere-like $\text{Pr}^{3+}:\text{LaF}_3$ ($C_{\text{Pr}} = 7\%$) NPs synthesized at 1:6 stoichiometric proportion of $\text{La}(\text{NO}_3)_3$, $\text{Pr}(\text{NO}_3)_3$, and NaF. Regardless of the stoichiometric proportion of $\text{La}(\text{NO}_3)_3$, $\text{Pr}(\text{NO}_3)_3$, and NaF, the same volumes of NaF and $\text{La}(\text{NO}_3)_3/\text{Pr}(\text{NO}_3)_3$ solutions, time of reactions, temperature, and pH values were used intentionally for all the samples. Hence, the main strategy of synthesis of both SLNPs and PLNPs is exactly the same except for one parameter: for SLNPs, the NaF solution was poured very swiftly to the $\text{La}(\text{NO}_3)_3$ and $\text{Pr}(\text{NO}_3)_3$ solution, and for PLNPs, the NaF solution was added dropwise. The 1:1 SLNPs were treated by microwave for 30, 90, and 180 min and are named 1:1 SLNPs 30 min MW, 1:1 SLNPs 90 min MW, and 1:1 SLNPs 180 min MW, respectively.

2.2. Coprecipitation Synthesis of $\text{Pr}^{3+}:\text{LaF}_3$ ($C_{\text{Pr}} = 7\%$) Nanoparticles Using Different Stoichiometric Proportion of Rare-Earth Nitrates and Fluorinating Agent and Microwave-Assisted Treatment of $\text{Pr}^{3+}:\text{LaF}_3$ ($C_{\text{Pr}} = 7\%$) Nanoparticles. In order to synthesize the $\text{Pr}^{3+}:\text{LaF}_3$ ($C_{\text{Pr}} = 7\%$), NPs 0.188 g of Pr_2O_3 and 2.500 g and La_2O_3 were added to 70 mL of 10% nitric acid in a glass beaker. The mixture was heated to 50°C and stirred for 45 min until a

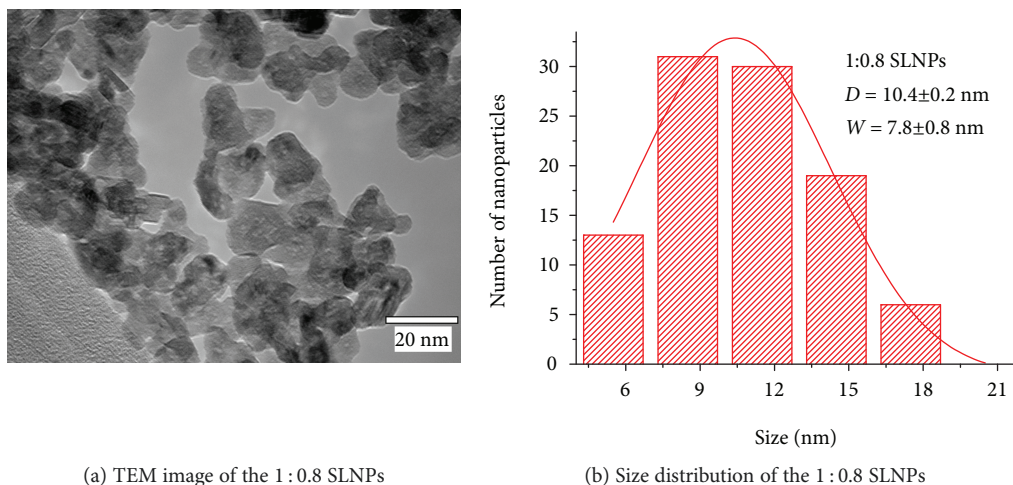


FIGURE 1

transparent light-green solution appeared. Then the mixture was filtered, poured in a polypropylene glass, and put on a magnetic mixer (400 revolutions per minute). The solutions of NaF were prepared by adding 0.836 g, 1.045 g, and 6.270 g of NaF into 160 mL of distilled water for 1:0.8, 1:1, and 1:6 stoichiometric proportions of $\text{La}(\text{NO}_3)_3$, $\text{Pr}(\text{NO}_3)_3$, and NaF, respectively. After filtration of the NaF solution, it was swiftly poured for SLNPs and added dropwise for PLNPs. Then the pH was adjusted to 4 by adding a 25% solution of ammonium hydrate. Then the mixture was stirring for 30 minutes (400 revolutions per minute) and then was washed by centrifugation (Janetski K24; 12000 RPM) using the deionized water for several times.

2.3. Microwave-Assisted Treatment of 1:1 SLNPs. The colloidal solutions of 1:1 SLNPs were divided into two volumes, and the first part was placed into a microwave oven (650 W, 2.45 GHz) for 30, 90, and 180 minutes. The resulting product was collected by centrifugation (Janetski K24; 12000 RPM) and washed using the deionized water for several times. Then NPs were dried in air.

2.4. Transmission Electron Microscopy and X-Ray Diffraction Experiments. The structure of the material was characterized by X-ray diffraction method (XRD) with Shimadzu XRD-7000S X-ray diffractometer. Analysis of samples was carried out in a transmission electron microscope Hitachi HT7700 Exalens. Sample preparation: 10 microliters of the suspension were placed on a formvar/carbon lacey 3 mm copper grid; drying was performed at room temperature. After drying, the grid was placed in a transmission electron microscope using a special holder for microanalysis. The analysis was held at an accelerating voltage of 100 kV in TEM mode.

2.5. Optical Spectroscopy. The luminescence spectra were recorded using CCD spectrometer (StellarNet), which detects the emission in 200–1100 nm spectral range with a spectral resolution of 0.5 nm. The optical parametric oscillator laser system (420–1200 nm) from JV LOTIS TII was used for

excitation of the luminescence of the samples. The pulse width and the pulse repetition rate were 10 ns and 10 Hz, respectively. The spectral width of laser radiation was less than 0.15 nm. The luminescent lifetimes of Pr^{3+} ions were detected using BORDO 211A (10 bit, 200 MHz bandwidth) digital oscillography and MDR-3 monochromator. The experiments were carried out at room temperature.

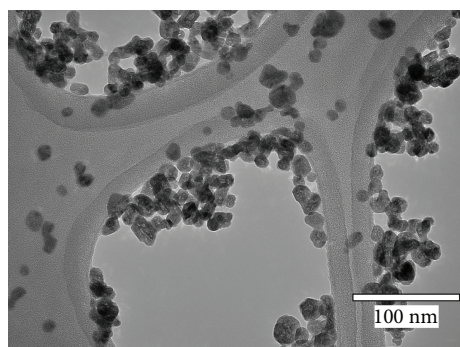
2.6. Elemental Analysis. Elemental analysis was carried out by using field-emission high-resolution scanning electron microscope Merlin Carl Zeiss with AZtec X-Max EDS system at accelerating voltage of incident electron of 20 kV and working distance of 10 mm. Excitation area is 1 μm .

Technique preparation: sample on chuck move in the chamber of vacuum apparatus Quorum Q 150T ES. Conductive layer apply by technique cathode sputtering using alloy Au/Pd by quantity proportion 80/20. The thickness of the alloy is 15 nm.

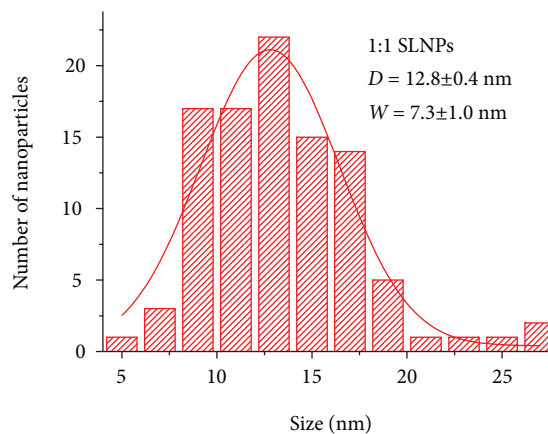
3. Results and Discussion

3.1. Transmission Electron Microscopy of the $\text{Pr}^{3+}:\text{LaF}_3$ ($C_{\text{Pr}} = 7\%$) Nanoparticles. According to the TEM data (Figures 1–6), all the samples differ between each other by size and shape. The size distribution histograms (insets of Figures 1–6) are fitted by Gaussian function from which diameter and a width of the size distribution are extracted. In order to build size distribution for the PLNPs, the length of each plate was measured. The values of diameter and width of size distribution are listed in Table 1.

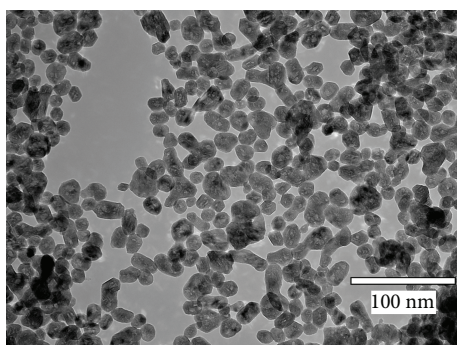
As can be seen from Figure 1, the 1:0.8 SLNPs have a relatively irregular shape. For the 1:1 SLNPs (Figure 2(a)), the shape is more regular. The 1:6 SLNPs (Figure 3) demonstrate the most regular shape among all the SLNPs. The average diameter of the SLNPs increases from 10.4 ± 0.2 to 16.5 ± 1.2 nm for 1:0.8 SLNPs and 1:6 SLNPs, respectively, with the increasing stoichiometric proportion of $\text{La}(\text{NO}_3)_3$, $\text{Pr}(\text{NO}_3)_3$, and NaF. For the SLNPs, the values of the width of the size distribution do not differ between each other significantly.



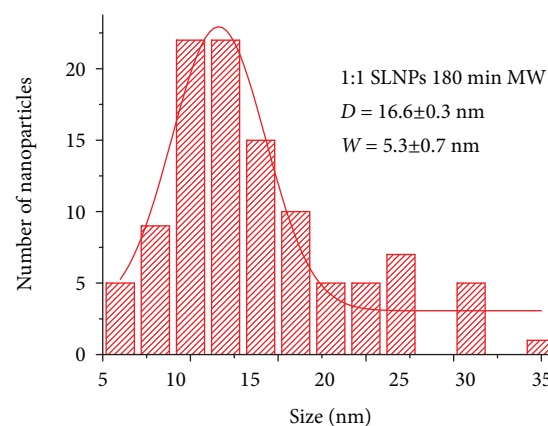
(a) TEM image of the 1 : 1 SLNPs



(b) Size distribution of the 1 : 1 SLNPs

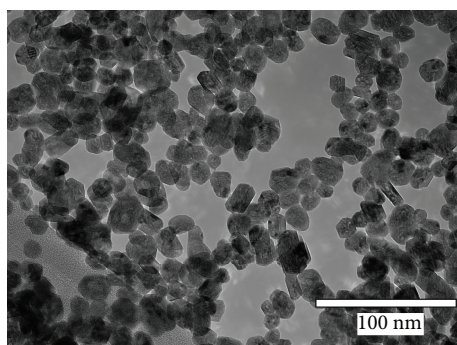


(c) TEM image of the 1 : 1 SLNPs treated by MW (180 min)

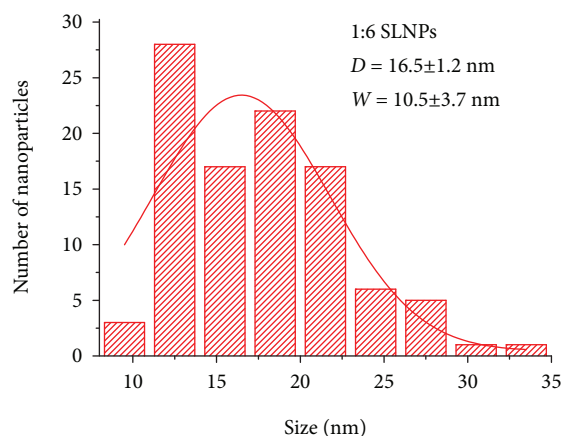


(d) Size distribution of the 1 : 1 SLNPs treated by MW (180 min)

FIGURE 2



(a) TEM image of the 1 : 6 SLNPs



(b) Size distribution of the 1 : 6 SLNPs

FIGURE 3

In the case of the SLNPs treated by MW, the regularity of the shape of the 1 : 1 SLNPs increases with the increasing time of MW treatment. The 1 : 1 SLNPs 180 min MW also demonstrated a relatively regular shape (Figure 2(b)) (the 1 : 1 SLNPs 30 min MW and 1 : 1 SLNPs 90 min MW are not shown for the sake of brevity). The value of size

distribution decreases with the increasing time of MW treatment which is in good accordance with the literature data [15, 17, 19, 20].

The shape of the PLNPs demonstrates a remarkable difference from the SLNPs. According to Figures 4 and 5, the 1:0.8 PLNPs and the 1:1 PLNPs form agglomerates

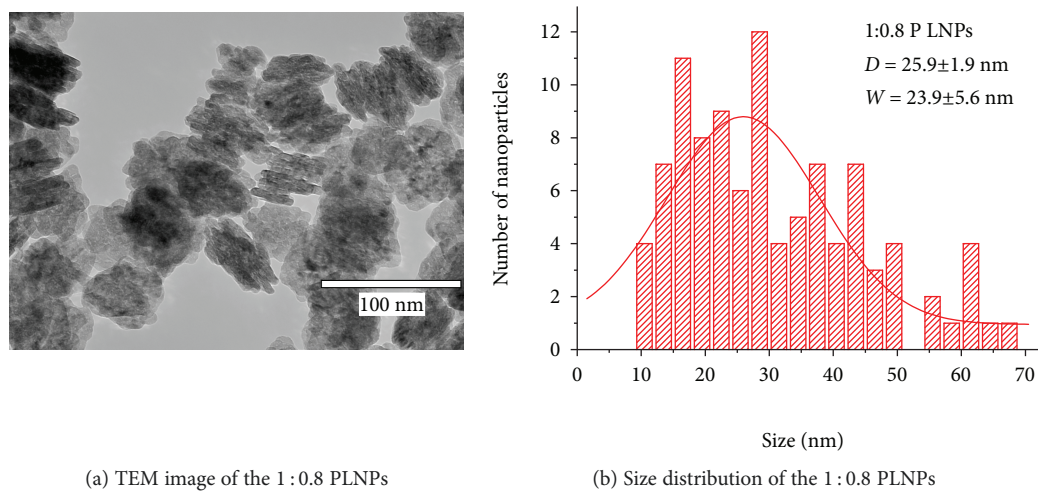


FIGURE 4

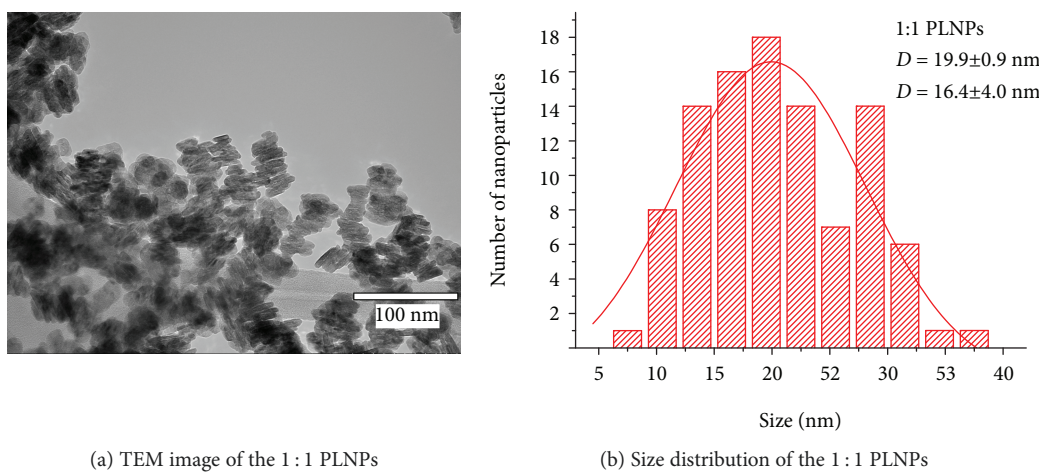


FIGURE 5

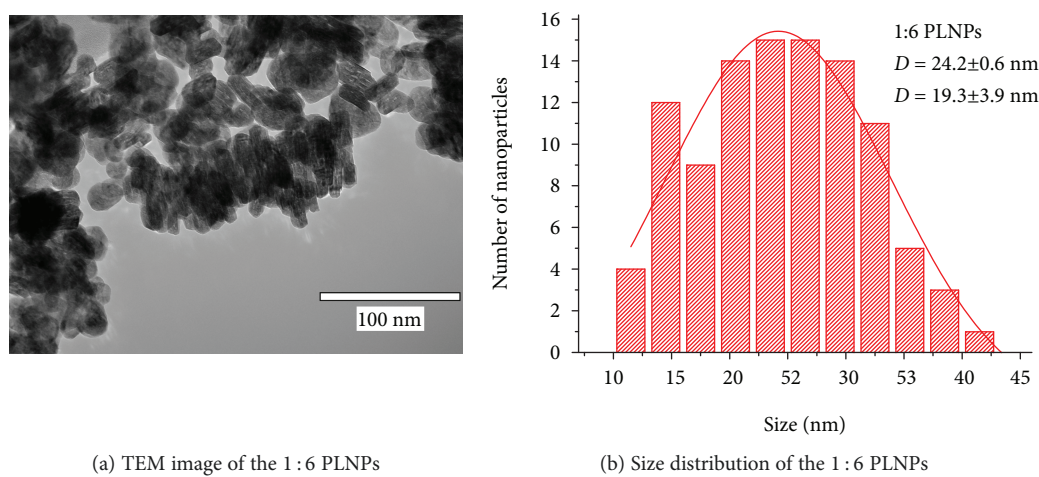


FIGURE 6

TABLE 1: The values of diameter (D) and width (W) of the size distribution of the samples.

Sample	D (nm) by TEM	W (nm) by TEM
1 : 0.8 PLNPs	25.9 ± 1.9	23.9 ± 5.6
1 : 1 PLNPs	19.9 ± 4.0	16.4 ± 4.0
1 : 6 PLNPs	24.2 ± 0.6	19.3 ± 3.9
1 : 0.8 SLNPs	10.4 ± 0.2	7.8 ± 0.8
1 : 1 SLNPs	12.8 ± 0.4	7.3 ± 1.0
1 : 6 SLNPs	16.5 ± 1.2	10.5 ± 3.7
1 : 1 SLNPs (30 min MW)	13.9 ± 0.7	8.9 ± 1.8
1 : 1 SLNPs (90 min MW)	15.0 ± 0.5	7.1 ± 1.2
1 : 1 SLNPs (180 min MW)	16.6 ± 0.3	5.3 ± 0.7

consisting of thin plates. The average thickness of the 1 : 0.8 PLNPs is around 4 nm. The edges of both the 1 : 0.8 PLNPs and the 1 : 1 PLNPs are rough. The values of the size distribution of the PLNPs are almost two times broader than that for the SLNPs. However, the 1 : 6 PLNPs are thicker (Figures 6(a) and 6(b)). Most of the 1 : 6 PLNPs are more similar to the SLNPs. It can be concluded that for the 1 : 0.8 PLNPs and the 1 : 1 PLNPs, the surface-to-volume ratio is higher than that of the rest of the NPs which can affect their optical properties [4] discussed in Optical Spectroscopy and Luminescence Lifetimes of the $\text{Pr}^{3+}:\text{LaF}_3$ ($C_{\text{Pr}} = 7\%$) Nanoparticles.

For all the samples mentioned above, the calculations of the crystallite sizes and lattice strains via Debye-Scherrer and Williamson-Hall methods were carried out. These calculations will be discussed in the next part of the article. However, one of the main conclusions made from microscopy data is that SLNPs are more isotropic in shape and, as a consequence, more appropriate for Debye-Scherrer and Williamson-Hall methods. For this reason, 1 : 1 SLNPs were chosen for further microwave- (MW-) assisted treatment in order to study the contribution of MW irradiation into physical properties of the NPs. Although the regularity of the shape of the 1 : 6 SLNPs is slightly higher, we did not use the 1 : 6 SLNPs intentionally because in the majority of the articles, the 1 : 1 stoichiometric proportions of rare-earth nitrates and fluorinating agent are used; hence, this information is more valuable.

It can be seen from Table 1 that the diameter of the 1 : 1 SLNPs increases with the increasing time of MW treatment. The value of size distribution becomes narrower from 10.5 ± 3.7 to 5.3 ± 0.7 nm for 0 and 180 min of MW treatment, respectively. The regularity of shape also improves with the increasing time of MW treatment.

The difference in size and shape of the PLNPs and the SLNPs can be explained by different synthesis conditions. In case of swift addition of NaF solution, the formation of the SLNPs is caused by homogeneous nucleation occurring when the concentration of rare earth and F^- ions becomes significantly higher than the equilibrium concentration immediately and the spontaneous growth of NPs takes place [30, 31]. In the case of dropwise addition, the fast increase of F^- ions concentration does occur. In such conditions,

the final shape of a nanocrystal can be determined by the growth competition of different crystal planes [32]. For hexagonal-phase materials, a specific morphology happens because of growth competition between the [001] planes and the [100] planes. Obviously, the PLNPs are preferentially generated if the growth rate of the [100] and [010] planes is higher than that of the [001] plane. For instance, in the case of the 1 : 0.8 PLNPs, the distance between two fringes which are parallel to the upper and lower pedestals of the plate is measured to be 0.35 nm which corresponds to the [002] plane of the LaF_3 crystal. This fact confirms the preferred growth along both the [100] and [010] planes under the existing conditions of synthesis. Moreover, the 1 : 6 PLNPs demonstrate more spherical shape comparing with the 1 : 0.8 and 1 : 1 SLNPs. It can be attributed to the 1 : 6 stoichiometric proportion of $\text{La}(\text{NO}_3)_3$, $\text{Pr}(\text{NO}_3)_3$, and NaF which leads to a more swift increase of F^- ions concentration, and the nature of the reaction looks similar to the reaction for the SLNPs.

3.2. X-Ray Diffraction and Elemental Analysis of the $\text{Pr}^{3+}:\text{LaF}_3$ ($C_{\text{Pr}} = 7\%$) Nanoparticles

3.2.1. Lattice Constant Calculation. The X-ray diffraction (XRD) patterns of the PLNPs, SLNPs, and SLNPs treated by MW irradiation and simulation are shown in Figures 7(a)–7(d), respectively. According to the XRD data, all the NPs are hexagonal-structured nanocrystals that correspond to the structure of matrixes of LaF_3 and PrF_3 . Sharp peaks and lack of peaks from impurities are observed, suggesting the high purity and good crystallinity of these samples. Also, the lack of amorphous phase was detected. For all the samples, the lattice parameters a and c are calculated using the formulas from [33, 34]. For all the samples, a and c are 0.7164 and 0.7330 nm, respectively. The lattice parameters for LaF_3 (JCPDS–32–0483) are $a = 0.7186$ and $c = 0.7352$ nm. The reduction of $\text{Pr}^{3+}:\text{LaF}_3$ lattice parameters apparently related to crystal lattice distortion. The radius of Pr^{3+} (0.105 nm) is smaller than that of La^{3+} (0.113 nm) due to the lanthanide contraction, so the cell volume of $\text{Pr}^{3+}:\text{LaF}_3$ reduces with more Pr^{3+} replacing La^{3+} [14].

3.2.2. Elemental Analysis. NaF is considered a very specific fluorinating agent. On the one hand, according to the literature data in some cases, the use of NaF leads to $\text{Sr}_{1-x}\text{Na}_x\text{F}_{2-x}$, $\text{Ca}_{1-x}\text{Na}_x\text{F}_{2-x}$ [35, 36], NaF-RF_3 , and/or NaRF_4 (where R = rare earth) [37] formation in water-based coprecipitation method. On the other hand, in spite of the possibility of NaF-RF_3 and/or NaRF_4 formation, the synthesis of NaF-LaF_3 and/or NaLaF_4 is considered as a very specific task. This is because La^{3+} has the largest cationic radius among the lanthanide ions, and the ionic bond of $\text{La}^{3+}-\text{F}^-$ is stronger than that of $\text{Na}^{+}-\text{F}^-$ and other $\text{RE}^{3+}-\text{F}^-$, as reflected by the melting points of several representatives: $\text{LaF}_3(1493^\circ\text{C}) > \text{NdF}_3(1410^\circ\text{C}) > \text{SmF}_3(1306^\circ\text{C}) > \text{TbF}_3(1231^\circ\text{C}) > \text{NaF}(993^\circ\text{C})$ [38]. As a result, in coprecipitation route, cations are difficult to settle into the lattice in compounds with large RE cations such as NaLaF_4 , which makes the synthesis of these compounds more difficult than that of NaYF_4 or NaLuF_4 [39].

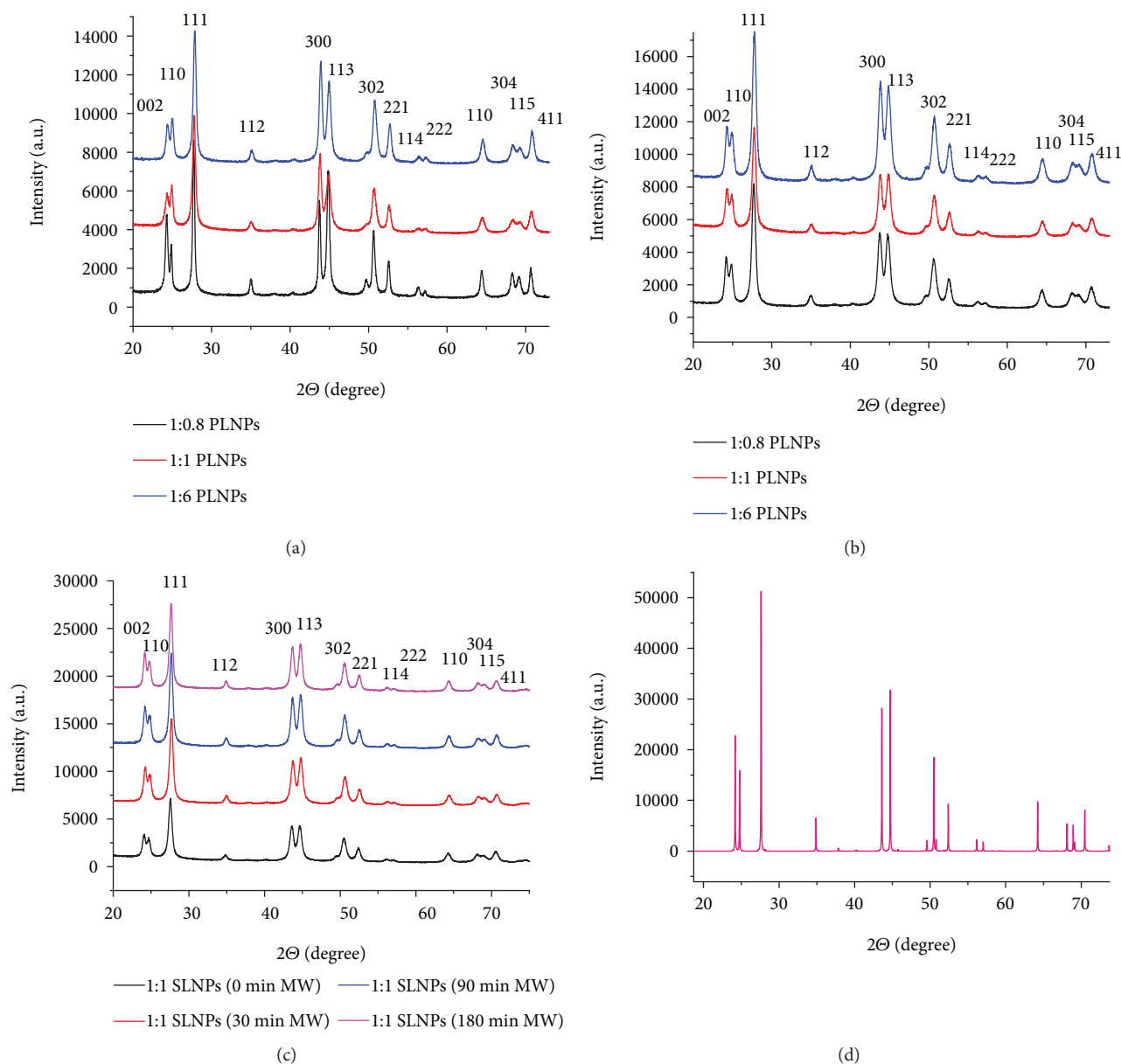


FIGURE 7: (a) XRD patterns of the PLNPs. (b) XRD patterns of the SLNPs. (c) XRD patterns of the SLNPs treated by MW. (d) Simulation of the LaF_3 XRD patterns.

For these reasons, NaLaF_4 compound is considered thermodynamically nonpreferred [39]. This fact results in the shortage of efficient synthetic methods for the preparation of pure β - NaLaF_4 nanocrystals [40]. Indeed, we failed to find a work devoted to low-temperature coprecipitation method of synthesis of pure NaLaF_4 NPs. On the other hand, in papers devoted to the synthesis and investigation of undoped and doped NaLaF_4 NPs, the high-temperature hydrothermal routes or melting in a corundum crucible are utilized [41, 42].

Moreover, it is noteworthy that the β - NaLaF_4 has a very distinguishable XRD pattern (diffraction peaks at 16.6, 28.9, 33.6, 37.7, 41.4, 44.9, 48.1, 51.3, 57.2, and 60.0° can be indexed to the planes (100), (110), (200), (111), (201), (120), (002), (300), (112), and (220), respectively) [43]. This pattern differs from the LaF_3 one. In the case of complex NaF-LaF_3 system,

the notable amount of NaLaF_4 would be detected via double-phase XRD pattern as it is observed in [43].

In our work, as it is mentioned above, we do not observe any impurity peaks. It can be suggested that there is no second β - NaLaF_4 phase or this phase is negligible and cannot be detected via our X-ray diffractometer.

On the other hand, a small amount of Na can form NaF-LaF_3 system without forming the second phase. Just in order to check the presence of Na in the samples, we have performed an elemental analysis. The elemental analysis revealed that all the samples do not contain sodium as well as other elements. The presence of Pr, La, and F was proved. The elemental analysis spectra of 1:0.8 PLNPs, 1:1 PLNPs, 1:6 PLNPs, 1:0.8 SLNPs, 1:1 SLNPs, 1:6 SLNPs, and 1:1 SLNPs 180 MW are shown in Figures 8(a)–8(g), respectively.

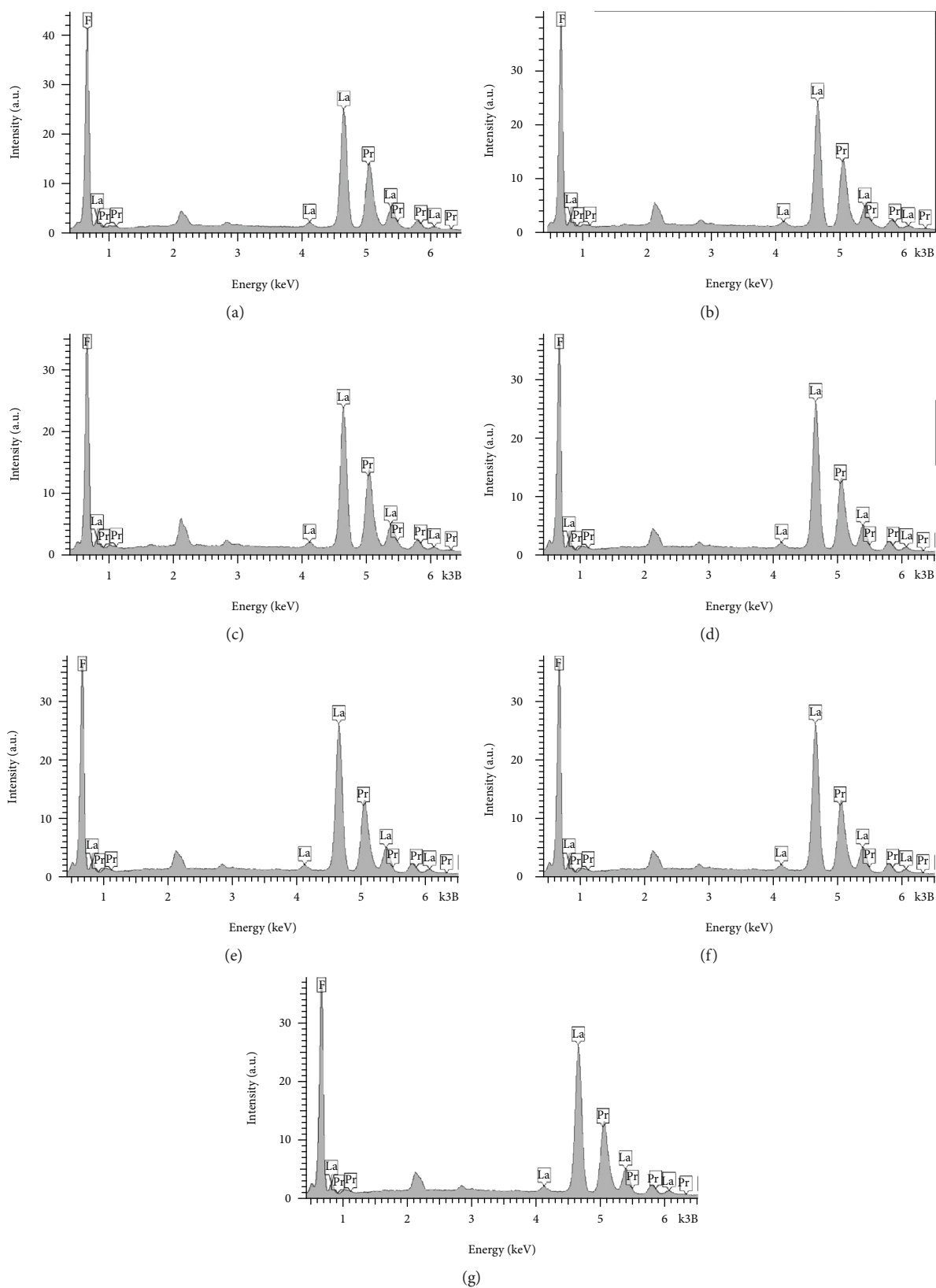


FIGURE 8: The elemental analysis spectra of 1:0.8 PLNPs (a), 1:1 PLNPs (b), 1:6 PLNPs (c), 1:0.8 SLNPs (d), 1:1 SLNPs (e), 1:6 SLNPs (f), and 1:1 SLNPs 180 MW (g). The unidentified peaks are the peaks of the conductive layer which were used for the sample preparation.

The unidentified peaks are the peaks of the conductive layer which was used for the sample preparation. The elemental analysis data are listed in Table 2.

3.2.3. Debye-Scherrer Calculations. The instrumental corrected broadening β_{hkl} corresponding to the diffraction peak of $\text{Pr}^{3+}:\text{LaF}_3$ was estimated using equation (1) [33, 34] as follows:

$$\beta_{\text{hkl}} = [(\beta_{\text{hkl}})_{\text{Measured}}^2 - (\beta_{\text{hkl}})_{\text{Instrumental}}^2]^{1/2}. \quad (1)$$

In order to estimate the average size of the NPs, the Debye-Scherrer method is used [44]:

$$D = \frac{K\lambda}{\beta_D \cos\theta}, \quad (2)$$

where D is a diameter of a NP, K is a shape factor (we used $K = 0.9$), λ is the X-ray wavelength (0.15418 nm), β_D is the line broadening at half the maximum intensity (FWHM) in radians, and θ is the Bragg angle (in degrees). The diffraction peaks having the lowest values of the signal-noise ratio are chosen. The values of D in different crystallography orientations (hkl) are listed in Tables 3 and 4. Also, Figures 9(a) and 9(b) summarize these data.

We do not compare TEM data and the Debye-Scherrer calculations of the D intentionally for some reasons. More specifically, equation (2) assumes that the peak broadening is related to the nanoscale dimensionality of the crystalline particles only. It does not take into control the presence of strains and distortions in NPs; hence, the presence of these strains and distortions can seriously confound the D value. More than that the size calculated via Debye-Scherrer formula is the size of coherently diffracting domains which is not generally the same as the particle size [24, 34]. Additionally, according to the microscopy data, all the samples have relatively broad size distribution (several nm) of NPs which require calculation of the additional constant for the Debye-Scherrer equation [45]. Also, according to the microscopy data, the shape of the NPs is far from perfect spherical or cubic; hence, the shape factor K is very sophisticated and actually should be calculated for each crystallographic orientation (hkl) [45]. The shape of both the PLNPs and the SLNPs is not perfect, and for all the samples, the shape factor K cannot be calculated precisely. The value of 0.9 is taken just in order to estimate the size of the particles. Summarizing all the above-mentioned information, it is very difficult to compare TEM data and Debye-Scherrer calculations. Hence, it is difficult to estimate the contribution of size into the peak broadening for all the samples in this study. For more precise results, the Williamson-Hall method described in the next part of the article is used.

On the one hand, the shape factor K depends on the crystallographic orientation (hkl) and the symmetry [45]. The symmetry is the same for all the samples; hence, it can be assumed that the K is a function of the crystallographic orientation (hkl) only. For irregular-shaped NPs,

TABLE 2: The elemental analysis data (weight %).

Sample	Pr	La	F
1 : 0.8 PLNPs	5.51	65.79	28.70
1 : 1 PLNPs	5.41	66.51	28.08
1 : 6 PLNPs	5.41	67.17	27.42
1 : 0.8 SLNPs	5.08	63.87	31.06
1 : 1 SLNPs	5.63	68.28	26.09
1 : 6 SLNPs	5.49	66.02	28.49
1 : 1 SLNPs (180 min MW)	6.04	71.17	22.79

the K is very sophisticated. For perfectly spherical NPs, the $K = 0.9$ and it is the same for all the crystallographic orientations, and the value of D does not depend on the crystallographic orientation. If the NPs are not perfectly spherical, the values of D differ between each other. The irregular-shaped NPs should have the values of D which differ between each other significantly.

The difference in D values can be estimated via standard deviation (SD) from the mean value of D . The values of D and the SD are listed in Tables 3 and 4 (see also Figures 9(a) and 9(b)). For the 1 : 0.8 PLNPs and the 1 : 1 PLNPs, the SD are 5.1 and 4.4, respectively, and these NPs are really irregular in shape. The rest of the samples demonstrate the SD around 1.5, and their shape is more regular and more spherical. The MW-treated NPs also demonstrate the SD around 1.5. Moreover, for the 1 : 0.8 PLNPs and the 1 : 1 PLNPs, the values of D_{002} is almost 2 times bigger than either D_{110} or D_{300} which corresponds to growth along [100] and [010] axis. These facts additionally confirm the microscopy data concerning irregularity in the shape of the 1 : 0.8 PLNPs and the 1 : 1 PLNPs.

This irregularity in shape can also be confirmed by assessing the linearity of the Debye-Scherrer formula. For this purpose, the Debye-Scherrer formula is rearranged.

$$\cos\theta = \frac{K\lambda}{D} \left(\frac{1}{\beta_D} \right). \quad (3)$$

The plots were drawn with $1/\beta_D$ on the x -axis and $\cos\theta$ along the y -axis. The K is assumed 0.9. The anisotropy in shape of the NPs leads to the phenomenon that the XRD peaks are broadened differently. As a consequence, the linearity of this plot can additionally confirm or disprove the isotropy of the shape of the NPs within the Debye-Scherrer model. If the shape of the NPs is far from spherical, the linearity of equation (3) should be low. The almost spherical NPs should demonstrate good linearity of equation (3). In turn, the linearity can be estimated using the Pearson coefficient. The values of the Pearson coefficient are listed in Tables 5 and 6. Taking into control that good linearity of data requires the values of Pearson coefficient more than 0.9, the comparison of the samples is performed. It is seen that the Debye-Scherrer data do not demonstrate perfect linearity especially for the 1 : 0.8 PLNPs and the 1 : 1 PLNPs

TABLE 3: The values of the size (D) of the NPs not treated by microwave irradiation in different crystallography orientations.

Peak (hkl)/ D (nm)	1 : 0.8 PLNPs	1 : 1 PLNPs	1 : 6 PLNPs	1 : 0.8 SLNPs	1 : 1 SLNPs	1 : 6 SLNPs
(002)	21.5	19.7	16.6	17.0	14.8	16.6
(110)	34.4	32.4	15.2	16.0	16.4	15.5
(111)	29.1	26.1	15.3	15.6	16.0	15.3
(112)	30.2	27.8	14.9	13.3	13.6	14.7
(300)	30.8	27.6	14.7	14.9	14.3	15.0
(113)	22.5	20.0	13.3	13.5	13.7	13.6
(302)	21.8	20.4	11.4	11.5	12.7	11.9
(221)	29.7	25.7	15.0	13.5	15.9	15.8
(223)	22.7	19.8	12.7	13.0	12.9	12.8
(115)	24.4	22.8	12.7	12.8	12.7	12.7
Mean D	25.5	24.2	14.2	14.3	14.2	14.4
Standard deviation	5.1	4.4	1.6	1.7	1.3	1.5

TABLE 4: The values of the size (D) of the NPs treated by MW irradiation in different crystallography orientations.

Peak (hkl)/ D (nm)	1 : 1 SLNPs	1 : 1 SLNPs (30 min MW)	1 : 1 SLNPs (90 min MW)	1 : 1 SLNPs (180 min MW)
(002)	14.8	15.8	16.1	19.7
(110)	16.4	17.2	17.4	19.7
(111)	16.0	16.3	16.8	18.4
(112)	13.6	16.0	16.6	18.5
(300)	14.3	14.5	15.7	16.6
(113)	13.7	14.2	14.9	16.4
(302)	12.7	12.8	13.7	13.8
(221)	15.9	15.6	16.0	19.0
(223)	12.9	13.2	13.9	14.9
(115)	12.7	13.2	13.9	14.8
Mean D	14.2	14.9	15.5	17.2
Standard deviation	1.3	1.5	1.3	1.8

which have low linearity (the Pearson coefficients are 0.72 and 0.71, respectively). Also, the values of D of the 1 : 0.8 PLNPs and the 1 : 1 PLNPs for different crystallography orientations differ between each other significantly comparing with the rest of the samples (Table 3). These facts indicate the anisotropy in shape of the 1 : 0.8 PLNPs and the 1 : 1 PLNPs which is also in agreement with microscopy data. However, the 1 : 1 SLNPs and the 1 : 6 SLNPs demonstrate relatively good linearity having the Pearson coefficient around 0.87.

In contrast to the above-mentioned samples, the 1 : 1 SLNPs treated by MW demonstrate the Pearson coefficient around 0.9 and more which confirms the conclusions based on microscopy data.

Summarizing all the above-mentioned information, the Debye-Scherrer model confirmed the anisotropy in shape of some samples. However, comparison of Debye-Scherrer

diameters and the TEM sizes seems to be difficult especially for the PLNPs. Hence, the contribution of the nanoscale dimensionality into the peak broadening is not clear.

In order to take into account both the nanoscale dimensionality of the NPs and lattice strain contribution into the peak broadening, the Williamson-Hall method is used.

3.2.4. The Williamson-Hall Calculations of Size and Strain. If the peak broadening is related to the presence of strains induced in powders due to crystal imperfection and distortion only, these strains are calculated using the equation as follows [34, 46]:

$$\varepsilon = \frac{\Delta d}{d} = \frac{\beta_s}{4tg\theta}, \quad (4)$$

where d is a distance between crystallographic planes, and the values of d are into an interval from $d - \Delta d$ to $d + \Delta d$.

Assuming that the particle size and strain contributions to line broadening are independent to each other, the observed line breadth is simply the sum of $\beta_D + \beta_s$ from equations (2) and (4).

$$\beta_{\text{hkl}} = \beta_D + \beta_s = \frac{K\lambda}{D\cos\theta} + 4\varepsilon t g\theta. \quad (5)$$

By rearranging the above equation, we get

$$\beta_{\text{hkl}} \cos\theta = \frac{K\lambda}{D} + 4\varepsilon t \sin\theta. \quad (6)$$

Equations (5) and (6) are the Williamson-Hall equations. A plot (equation (6)) is drawn with $4\sin\theta$ along the x -axis and $\beta_{\text{hkl}} \cos\theta$ along the y -axis. From the linear fit to the data, the crystalline size was estimated from the y -intercept, and the strain ε , from the slope of the fit. The Williamson-Hall plots for the SLNPs and the PLNPs are shown in Figure 10(a). The Williamson-Hall method assumes that the particles are isotropic in shape and the size of strains in different crystallographic directions are similar

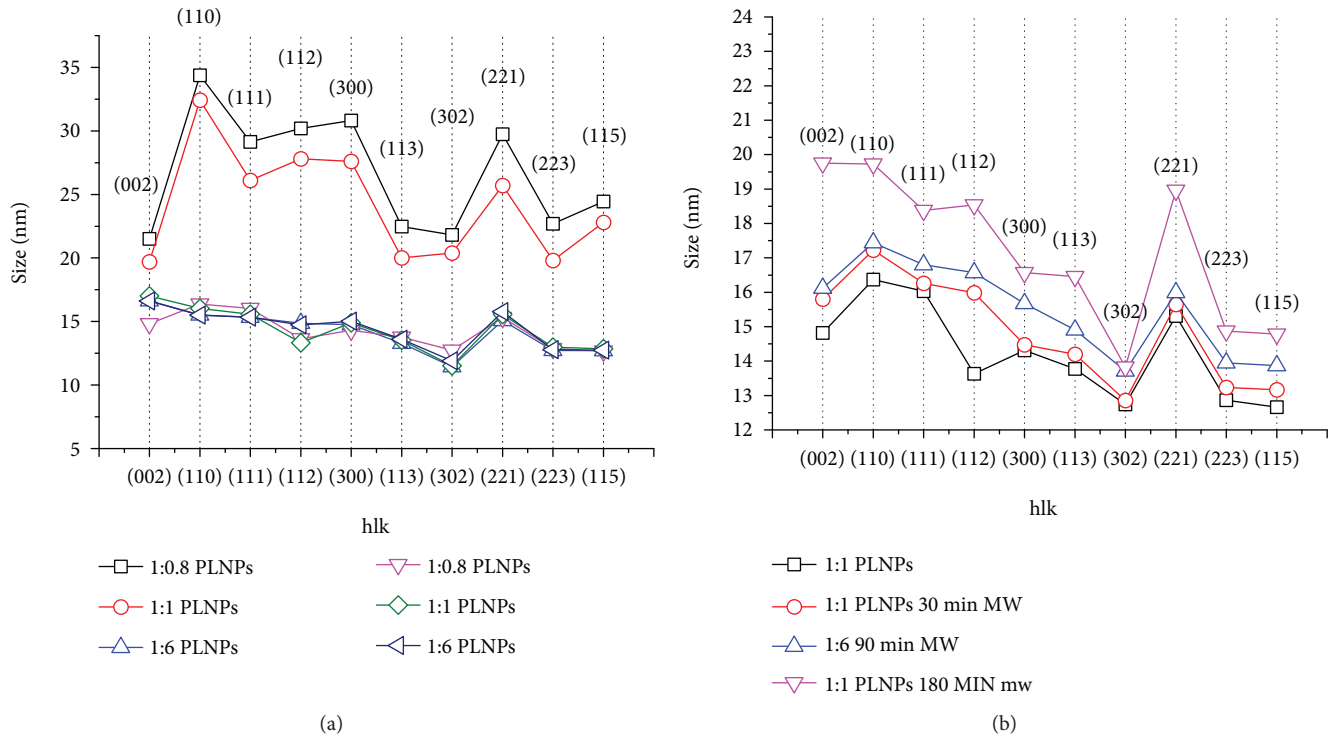


FIGURE 9: (a) The Debye-Scherrer size of the NPs in different crystallography orientations. (b) The Debye-Scherrer size of the NPs subjected to microwave treatment in different crystallography orientations.

TABLE 5: The values of the diameter D and strain ε of the samples calculated via TEM data, Debye-Scherrer (D-S), and Williamson-Hall (W-H) equations.

Sample	D (nm) by TEM	D_{111} (nm) by D-S	D (nm) by W-H	ε ($\times 10^{-4}$) by W-H
1:0.8 PLNPs	25.9 ± 1.9	29.1	36.5 ± 8.4	11 ± 5
1:1 PLNPs	19.9 ± 4.0	26.1	29.4 ± 3.3	13 ± 4
1:6 PLNPs	24.2 ± 0.6	15.3	18.7 ± 1.9	15 ± 6
1:0.8 SLNPs	10.4 ± 0.2	15.6	18.5 ± 2.2	16 ± 5
1:1 SLNPs	12.8 ± 0.4	16.0	15.5 ± 1.7	13 ± 4
1:6 SLNPs	16.5 ± 1.2	15.3	18.4 ± 1.2	15 ± 5

TABLE 6: The values of the diameter D and strains ε of the samples calculated via Debye-Scherrer (D-S) and Williamson-Hall (W-H) equations.

Sample	D (nm) by TEM	D_{111} (nm) by D-S	D (nm) by W-H	ε ($\times 10^{-4}$) by W-H
1:1 SLNPs	12.8 ± 0.4	16.0	15.5 ± 1.7	13 ± 2
1:1 SLNPs (30 min MW)	13.9 ± 0.2	16.3	19.1 ± 1.5	15 ± 3
1:1 SLNPs (90 min MW)	15.1 ± 0.3	16.8	20.1 ± 0.9	12 ± 2
1:1 SLNPs (180 min MW)	16.6 ± 0.3	18.4	24.2 ± 1.2	15 ± 3

[47]. The TEM data, Debye-Scherrer, and Williamson-Hall calculations are listed in Table 5.

According to the microscopy data and the Debye-Scherrer calculations, the 1:0.8 PLNPs and the 1:1 PLNPs are highly anisotropic in shape. The SLNPs also are not perfectly isotropic. Hence, the accuracy of the Williamson-Hall calculations is not supposed to be high for at least 1:0.8 PLNPs and 1:1 PLNPs. However, the SLNPs treated by MW irradiation demonstrate relatively good shape isotropy; hence, the Williamson-Hall method is more applicable for them. Here, we analyze size and strain as well as estimate applicability of the Williamson-Hall method by assessing the linearity of the Williamson-Hall plots.

As it is mentioned above, we do not quantitatively compare the TEM data and the Debye-Scherrer calculations. However, both Debye-Scherrer and Williamson-Hall calculations do not reflect such an important tendency as increasing of the sizes of the SLNPs with increasing stoichiometric proportion of rare-earth salts and NaF qualitatively. Actually, all the SLNPs are around 14.2 nm in diameter. This fact brings into a question the applicability of the Williamson-Hall method toward the samples. Indeed, it was already mentioned that in the Williamson-Hall method, it is assumed that the particles are isotropic in shape and the strain is uniform in different directions leading to independent crystal properties [33]. Analyzing the microscopy data and the Pearson coefficients for the Williamson-Hall plots, it can be concluded that irregularity in the shape of the NPs correlates with the Pearson coefficients for the Williamson-Hall plots (Table 7). Moreover,

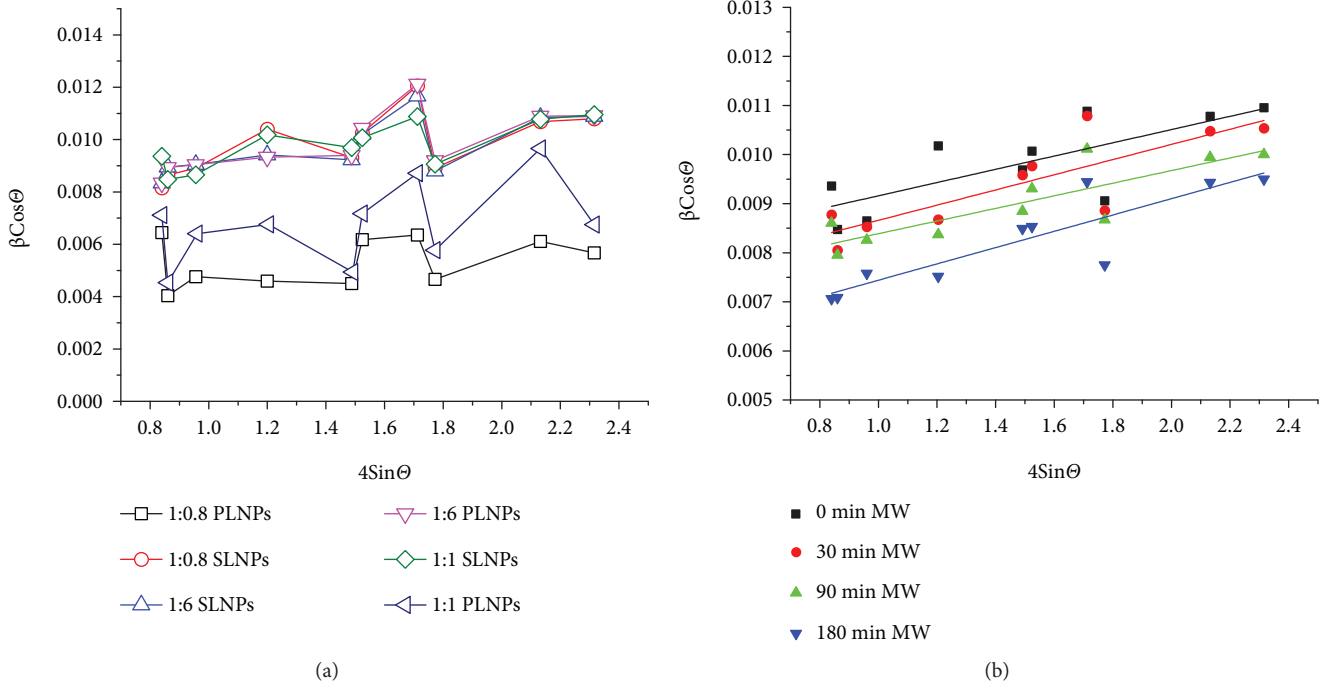


FIGURE 10: (a) The Williamson-Hall plot of the samples. Fit to the data, the strain is extracted from the slope and the crystalline size is extracted from the y-intercept of the fit. (b) The Williamson-Hall plot of the samples. Fit to the data, the strain is extracted from the slope and the crystalline size is extracted from the y-intercept of the fit.

TABLE 7: The values of the Pearson coefficient of the PLNP and the SLNPs.

Sample	1 : 0.8 PLNPs	1 : 1 PLNPs	1 : 6 PLNPs	1 : 0.8 SLNPs	1 : 1 SLNPs	1 : 6 SLNPs
Debye-Scherrer	0.72	0.71	0.87	0.82	0.88	0.87
Williamson-Hall	0.57	0.66	0.72	0.66	0.76	0.73

the accuracy and quality of the Williamson-Hall calculation seem to be dependent on the linearity of the plots.

It is seen that the most irregular-shaped 1:0.8 PLNPs and 1:1 PLNPs have very poor linearity (the Pearson coefficients are 0.57 and 0.66, respectively). The Pearson coefficient increases with improving the regularity of the shape of the NPs. Summarizing the above-mentioned information, the Williamson-Hall calculations of the diameter do not reflect tendencies of increasing the sizes of the SLNPs, and the Pearson coefficients are less than 0.9. It can be concluded that all the samples synthesized via coprecipitation method are not isotropic enough. On the other hand, in the specified accuracy, the values of strain ϵ seem to be equal for all the samples. Hence, the different conditions of the coprecipitation method do not lead to significant changing of the values of strain.

However, for the 1:1 SLNPs treated by MW for 30, 90, and 180 min (named 1:1 SLNPs 30 min, 1:1 SLNPs 90 min, and 1:1 SLNPs 180 min, respectively), both the Debye-Scherrer and Williamson-Hall methods reflect the tendency of increasing the sizes of the SLNPs with the increasing of MW treatment time (Table 6). The Williamson-Hall plots of the samples are shown in Figure 10(b).

Moreover, the Pearson coefficients for both Debye-Scherrer and Williamson-Hall plots of NPs treated with MW are equal or more than 0.9 (Table 8). Here, we try to assess how anisotropy in shape assessed via TEM influences the applicability of the Debye-Scherrer and Williamson-Hall theories by comparing the Pearson coefficients of linear fitting (Table 8).

It means that the Williamson-Hall model is more appropriate for the analysis of the samples treated by MW unlike the rest of the samples. For MW-treated NPs, the values of ϵ seem to be similar for all the samples within the accuracy. These values do not depend on the time of MW treatment. The values of ϵ are around 14×10^{-4} . These values are of the same magnitude to the results for ZnO NPs obtained in [24].

In the Williamson-Hall method, the value of ϵ seems to be similar for all the samples within the accuracy and does not depend on the time of MW treatment. It is reported in [15, 17, 48] that MW treatment improves the crystallinity of PrF_3 , DyF_3 , and LaF_3 NPs, respectively. As it is mentioned above, the growth mechanism of NPs during MW treatment is dissolution-recrystallization. Probably during 30, 90, and 180 min of MW treatment, the complete recrystallization does not occur. The average size of the NPs increases but

TABLE 8: The values of the Pearson coefficient of the SLNPs treated by MW.

Sample	1 : 1 SLNPs	1 : 1 SLNPs (30 min MW)	1 : 1 SLNPs (90 min MW)	1 : 1 SLNPs (180 min MW)
Debye-Scherrer	0.88	0.91	0.94	0.92
Williamson-Hall	0.76	0.90	0.93	0.91

significant reduction of strains does not take place during the chosen time of MW treatment. On the other hand, even 30 min of MW treatment makes the NPs more isotropic in shape, and the Pearson coefficient for 1 : 1 SLNPs and 1 : 1 SLNPs (30 min MW) increases from 0.76 to 0.90, respectively, which means that the isotropy of the shape of the NPs is improved and they become more appropriate for theoretical calculations via chosen methods. The values of the Pearson coefficient for all the samples subjected to MW treatment are equal to 0.90 or more which indicate the good linear approximation of the data. Also, based on the TEM data, it can be concluded that the shape of the NPs subjected to MW treatment is more regular and spherical. The literature data for trifluoride NPs also confirm these results [15, 17]. It means that the NPs subjected to MW treatment are more appropriate for theoretical analysis via Williamson-Hall method comparing to the 1 : 0.8 PLNP and the 1 : 1 PLNPs demonstrating the most irregular shape and the broadest size distribution and, as a consequence, smaller values of the Pearson coefficient.

Finally, it is noteworthy to say that the Debye-Scherrer diameters are less than the Williamson-Hall ones which is in accordance with [47]. In this case, the Debye-Scherrer formula provides only a lower bound for the crystallite size. The Williamson-Hall diameter for all the particles is bigger than TEM diameter which can be explained by the wide variety of mechanisms leading to the peak broadening. These mechanisms are not taken into consideration within these models.

3.3. Optical Spectroscopy and Luminescence Lifetimes of the $\text{Pr}^{3+}:\text{LaF}_3$ ($C_{\text{Pr}} = 7\%$) Nanoparticles. Although the initial chemical composition of all the $\text{Pr}^{3+}:\text{LaF}_3$ ($C_{\text{Pr}} = 7\%$) samples is equal, some optical properties of the NPs differ from each other. On the one hand, the luminescence spectra of all the $\text{Pr}^{3+}:\text{LaF}_3$ NPs do not differ between each other. Figure 11(a) shows the spectra of the most distinguishable NPs. The transitions were determined according to [49]. The luminescent spectra have the emission bands at about 487, 523, 537, 580, 601, and 672 nm which are interpreted as a result of the transition from the $^3\text{P}_j$ ($j = 0, 1, 2$) excited states to $^3\text{H}_4$, $^3\text{H}_5$, $^3\text{H}_6$, and $^3\text{F}_3$ states of Pr^{3+} ions, respectively. The emission from the $^1\text{D}_2$ state was not found under the excitation condition and at the studied temperature range. Probably the emission from $^1\text{D}_2$ is not observed because of the lack of nonradiative relaxation of $^3\text{P}_j$ to $^1\text{D}_2$ due to low cutoff phonon frequency in LaF_3 (350–400 cm^{-1}).

On the other hand, the lifetime curves of $^3\text{P}_0$ state of Pr^{3+} ions for different samples differ from each other notably

(Figures 11(b)–11(d)). In addition, luminescence lifetime curves are not one or double exponential. The fitting curves are more sophisticated. Since the theoretical description of lifetime curves seems to be difficult and lays behind the scope of this article, we qualitatively compare the lifetime curves between each other. It is seen from Figures 11(b) and 11(c) that the SLNPs demonstrate longer lifetime comparing with the suitable PLNPs. Moreover, for both the SLNPs and the PLNPs, the lifetime increases with increasing of the NPs size. The SLNPs treated by MW demonstrate the same tendency. The increasing of MW treatment time leads to increasing in lifetime (Figure 11(d)).

It can be suggested that the optical properties of the samples are mainly affected by the size and shape of the NPs and, as consequent, the volume-to-surface ratio [50, 51]. In this case, probably the main mechanism of luminescence quenching is related to energy multiphonon transfer from the excited ion to the high-vibronic energy molecule such as OH group adsorbed on the NPs surface [16, 52]. The thinnest 1 : 0.8 PLNPs having the biggest surface-to-volume ratio demonstrate the lowest luminescence lifetime which can be attributed to the proximity of the highest amount of Pr^{3+} ions to the surface OH groups which can be regarded as the main quenching centers in this system [53]. In [54], it is shown that the shape of rare-earth-doped dielectric NPs can affect the luminescence lifetime. Moreover, it is shown in [55] that the use of water-based coprecipitation method leads to the presence of OH groups into the NP's core as well. Hence, in the case of the MW-treated samples, the lifetime increasing can be attributed by two processes. The first is the increasing in size of the NPs which leads to a reduction of the role of the surface. The second is the migration of the OH groups from the NP's core to specific water clusters [30, 56, 57] which leads to reducing the total amount of Pr^{3+} ions contacting with OH groups.

The theoretical description of the decay curves is behind the scope of the article. In order to estimate and compare the specific lifetimes, we calculated the effective decay time, τ_{eff} , via equation (7) which is commonly used for such complicated nonexponential decay curves [58]:

$$\tau_{\text{eff}} = \frac{\int_0^\infty tI(t)dt}{\int_0^\infty I(t)dt}, \quad (7)$$

where $I(t)$, intensity; t , time. Values of the effective lifetime are listed in Table 9.

4. Conclusions

The 1 : 0.8 PLNPs, 1 : 1 PLNPs, 1 : 6 PLNPs, 1 : 0.8 SLNPs, 1 : 1 SLNPs, and 1 : 6 SLNPs were synthesized via coprecipitation method. The 1 : 1 SLNPs 30 min MW, 1 : 1 SLNPs 90 min MW, and 1 : 1 SLNPs 180 min MW were synthesized via coprecipitation method with subsequent MW treatment. All the samples were characterized by TEM and XRD. For all the samples, optical spectroscopy experiments were carried out. The XRD data were analyzed via the Debye-Scherrer and the Williamson-Hall methods.

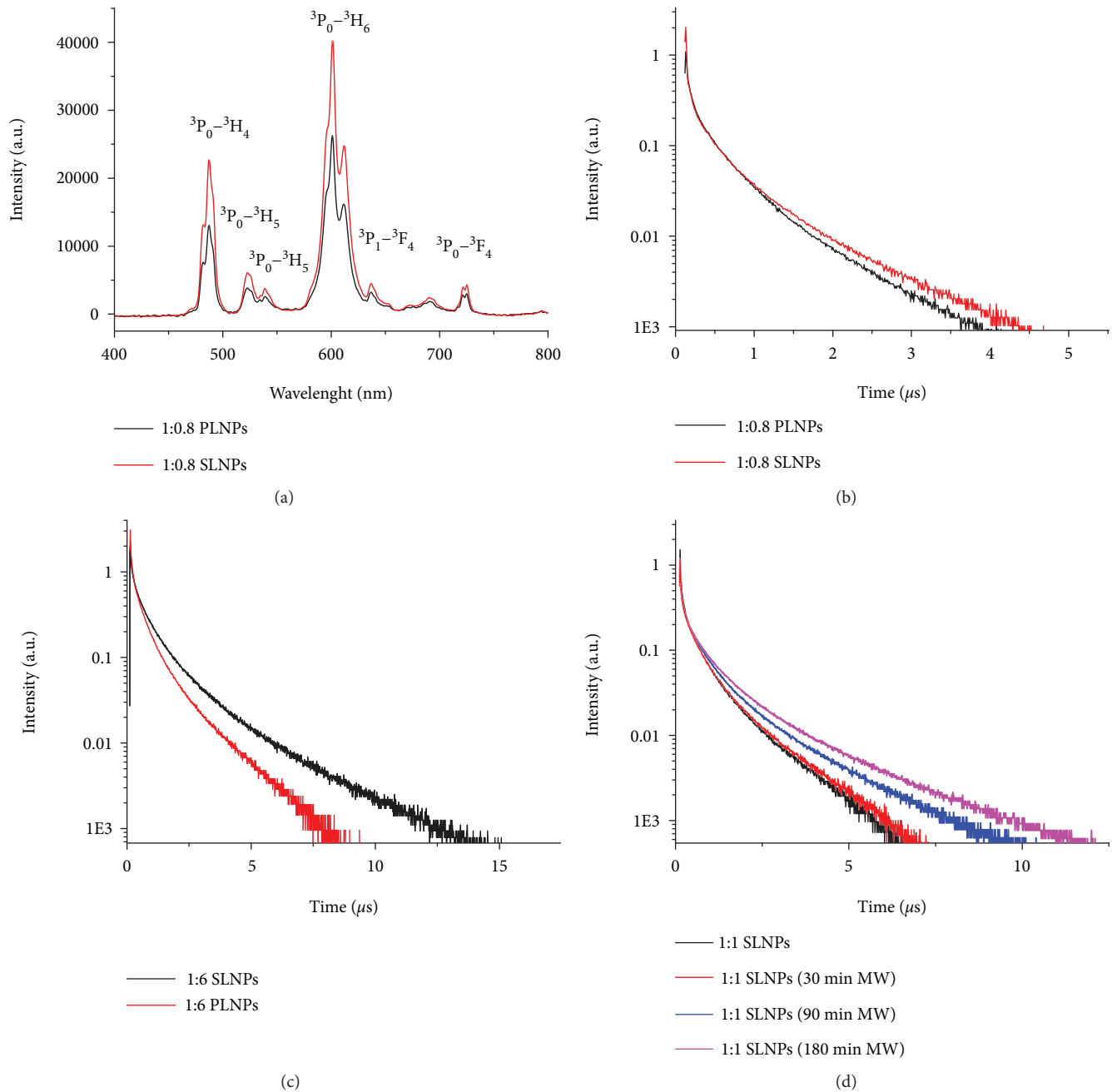


FIGURE 11: (a) Luminescence spectrum of 1 : 0.8 PLNPs and 1 : 8 SLNPs. (b) Lifetime curves of 1 : 0.8 SLNPs and 1 : 0.8 PLNPs. (c) Lifetime curves of 1 : 6 SLNPs and 1 : 6 PLNPs. (d) Lifetime curves of the SLNPs treated by MW.

It was revealed that the way of mixing the $\text{La}(\text{NO}_3)_3$, $\text{Pr}(\text{NO}_3)_3$, and NaF solutions strongly affects the shape of the NPs. The slow dropwise addition of the NaF solution to the $\text{La}(\text{NO}_3)_3$ and $\text{Pr}(\text{NO}_3)_3$ solution leads to the PLNPs formation; otherwise, the swift addition of the NaF solution leads to the formation of more spherical NPs (SLNPs).

The stoichiometric proportion of $\text{La}(\text{NO}_3)_3$, $\text{Pr}(\text{NO}_3)_3$, and NaF also strongly affects the size and the shape of the NPs. In the case of SLNPs, the size and regularity in shape of the SLNP increase with the increasing stoichiometric proportion of $\text{La}(\text{NO}_3)_3$, $\text{Pr}(\text{NO}_3)_3$, and NaF from 1 : 0.8 to 1 : 6. The increasing stoichiometric proportion of $\text{La}(\text{NO}_3)_3$,

$\text{Pr}(\text{NO}_3)_3$, and NaF also affect the PLNPs leading to an increase in thickness of the PLNPs. In the case of the PLNPs, the growth along the [100] and [010] planes occur more effectively than along the [001] plane which leads to PLNPs formation.

The size and regularity in shape of the SLNPs increase with the increasing time of MW treatment.

The Debye-Scherrer calculations have shown that the size of the most irregular-shaped 1 : 0.8 PLNPs and 1 : 1 PLNPs strongly depends on the crystallographic plane which additionally confirmed the shape irregularity of these NPs. The values of the diameter were calculated for several [hkl]

TABLE 9: The values of the effective lifetime τ_{eff} .

Sample	τ_{eff} (μsec)
1 : 0.8 PLNPs	0.54
1 : 1 PLNPs	0.64
1 : 6 PLNPs	0.82
1 : 0.8 SLNPs	0.60
1 : 1 SLNPs	0.71
1 : 6 SLNPs	1.17
1 : 1 SLNPs (30 min MW)	0.79
1 : 1 SLNPs (90 min MW)	0.89
1 : 1 SLNPs (180 min MW)	1.02

planes. For the 1 : 0.8 PLNPs and the 1 : 1 PLNPs, the SD of the values of size are 5.1 and 4.4, respectively. The rest of the samples demonstrate the SD around 1.5, and their shape is more regular and more spherical. The NPs treated by MW also demonstrate the SD around 1.5.

The Williamson-Hall method has shown that the values of strains are almost similar for all the samples (around 14×10^{-4}).

Optical spectroscopy experiments revealed that although all the samples have an equal chemical composition, the luminescence lifetimes for different samples differ between each other. The luminescence lifetime of the PLNPs is less than that of the SLNPs having an equal stoichiometric proportion of $\text{La}(\text{NO}_3)_3$, $\text{Pr}(\text{NO}_3)_3$, and NaF. The luminescence lifetime of the 1 : 1 SLNPs increases with the increasing time of MW treatment. Commonly, the lifetime increase with the increasing size of the NPs. Hence, the role of surface-quenching agents reduces. However, the luminescence lifetime curves cannot be fitted exponentially, and the additional theoretical interpretation is required. This last task is behind the scope of this work.

Data Availability

The TEM microscopy, XDR, spectra, and lifetime data used to support the findings of this study have been deposited in the Google disk repository (<https://drive.google.com/file/d/1D9RSIQwNOBqElv7tSfZ1EYJomr0cFbGk/view?usp=sharing>). The size distribution, Debye-Scherrer, Williamson-Hall, and elemental analysis data used to support the findings of this study are included within the article. These data are available upon request from the corresponding author.

Conflicts of Interest

The authors declare that they have no conflicts of interest.

Authors' Contributions

M. S. Pudovkin, D. A. Koryakovtseva, S. L. Korableva, and E. V. Lukinova have performed the synthesis. M. S. Pudovkin has performed all the calculations of the XRD data and written the manuscript. A. G. Kiiamov has performed the XRD experiments and XRD simulations. M. S. Pudovkin, R. Sh.

Khusnutdinova, A. S. Nizamutdinov, and V. V. Semashko have performed the optical spectroscopy experiments. S. L. Korableva, A. S. Nizamutdinov, and V. V. Semashko have made important remarks and gave feedback concerning the manuscript. All the authors have taken part in the discussion of the results.

Acknowledgments

The microscopy study was funded by the subsidy of the Russian Government (02.A03.21.0002) to support the Program of Competitive Growth of KFU among the World's Leading Academic Centers. The rest of the works was supported by the subsidy allocated to KFU for the state assignment in the sphere of scientific activities (3.1156.2017/4.6, 3.5835.2017/6.7). Microscopy studies were carried out at the Interdisciplinary Center of Analytical Microscopy of Kazan Federal University. We thank V. G. Evtugyn and V. Vorobev for performing the TEM microscopy and elemental analysis, respectively.

Supplementary Materials

The graphical abstract expresses the main idea of the article. Dropwise addition of the NaF solution to the $\text{Pr}(\text{NO}_3)_3$ and $\text{La}(\text{NO}_3)_3$ solution provides plate-like nanoparticles formation unlike the swift addition of the NaF solution to the $\text{Pr}(\text{NO}_3)_3$ and $\text{La}(\text{NO}_3)_3$ solution providing spherical-like nanoparticles formation. The luminescence lifetime of Pr ions in plate-like nanoparticles is less than the luminescence lifetime of Pr ions in spherical-like nanoparticles. The microwave treatment of the spherical-like nanoparticles leads to increasing of their sizes and the luminescence lifetimes of Pr ions. (*Supplementary Materials*)

References

- [1] A. M. Gazizulina, E. M. Alakshin, E. I. Baibekov et al., "Electron paramagnetic resonance of Gd^{3+} ions in powders of $\text{LaF}_3:\text{Gd}^{3+}$ nanocrystals," *JETP Letters*, vol. 99, no. 3, pp. 149–152, 2014.
- [2] E. Alakshin, A. Klochkov, S. Korableva et al., "Magnetic properties of powders LiTbF_4 and TbF_3 ," *Magnetic Resonance in Solids Electronic Journal*, vol. 18, no. 2, pp. 1–6, 2016.
- [3] D. Bekah, D. Cooper, K. Kudinov et al., "Synthesis and characterization of biologically stable, doped LaF_3 nanoparticles co-conjugated to PEG and photosensitizers," *Journal of Photochemistry and Photobiology A: Chemistry*, vol. 329, pp. 26–34, 2016.
- [4] Z. Xiaoting, T. Hayakawa, Y. Ishikawa, Y. Liushuan, and M. Nogami, "Structural investigation and Eu^{3+} luminescence properties of $\text{LaF}_3:\text{Eu}^{3+}$ nanophosphors," *Journal of Alloys and Compounds*, vol. 644, pp. 77–81, 2015.
- [5] E. C. Ximendes, U. Rocha, K. U. Kumar, C. Jacinto, and D. Jaque, " LaF_3 core/shell nanoparticles for subcutaneous heating and thermal sensing in the second biological-window," *Applied Physics Letters*, vol. 108, no. 25, article 253103, 2016.
- [6] H. Dong, S. Du, X. Zheng et al., "Lanthanide nanoparticles: from design toward bioimaging and therapy," *Chemical Reviews*, vol. 115, no. 19, pp. 10725–10815, 2015.

- [7] Y. Tang, H. Xin, F. Yang, and X. Long, "A historical review and bibliometric analysis of nanoparticles toxicity on algae," *Journal of Nanoparticle Research*, vol. 20, no. 4, 2018.
- [8] P. P. Fedorov, A. A. Luginina, S. V. Kuznetsov, and V. V. Osiko, "Nanofluorides," *Journal of Fluorine Chemistry*, vol. 132, no. 12, pp. 1012–1039, 2011.
- [9] D. Jaque and F. Vetrone, "Luminescence nanothermometry," *Nanoscale*, vol. 4, no. 15, pp. 4301–4326, 2012.
- [10] C. D. S. Brites, P. P. Lima, N. J. O. Silva et al., "Thermometry at the nanoscale," *Nanoscale*, vol. 4, no. 16, pp. 4799–4829, 2012.
- [11] U. Rocha, K. U. Kumar, C. Jacinto et al., "Neodymium-doped LaF_3 nanoparticles for fluorescence bioimaging in the second biological window," *Small*, vol. 10, no. 6, pp. 1141–1154, 2014.
- [12] P. Rahman and M. Green, "The synthesis of rare earth fluoride based nanoparticles," *Nanoscale*, vol. 1, no. 2, pp. 214–224, 2009.
- [13] F. Wang and X. Liu, "Recent advances in the chemistry of lanthanide-doped up-conversion nanocrystals," *Chemical Society Reviews*, vol. 38, no. 4, pp. 976–989, 2009.
- [14] M. S. Pudovkin, P. V. Zelenikhin, V. Shtyryeva et al., "Coprecipitation method of synthesis, characterization, and cytotoxicity of $\text{Pr}^{3+}:\text{LaF}_3$ (CPr = 3, 7, 12, 20, 30%) nanoparticles," *Journal of nanotechnology*, vol. 2018, Article ID 8516498, 9 pages, 2018.
- [15] E. M. Alakshin, R. R. Gazizulin, A. V. Klochkov et al., "Annealing of PrF_3 nanoparticles by microwave irradiation," *Optics and Spectroscopy*, vol. 116, no. 5, pp. 721–723, 2014.
- [16] J. K. Krebs, S. P. Feofilov, A. A. Kaplyanskii, R. I. Zakharchenya, and U. Happek, "Non-radiative relaxation of Yb^{3+} in highly porous $\gamma\text{-Al}_2\text{O}_3$," *Journal of Luminescence*, vol. 83–84, pp. 209–213, 1999.
- [17] E. M. Alakshin, A. V. Klochkov, E. I. Kondratyeva et al., "Microwave-assisted hydrothermal synthesis and annealing of DyF_3 nanoparticles," *Journal of nanomaterials*, vol. 2016, article 7148307, 5 pages, 2016.
- [18] L. Wang and Y. Li, "Controlled synthesis and luminescence of lanthanide doped NaYF_4 nanocrystals," *Chemistry of Materials*, vol. 19, no. 4, pp. 727–734, 2007.
- [19] L. Ma, W.-X. Chen, Y.-F. Zheng, J. Zhao, and Z. Xu, "Microwave-assisted hydrothermal synthesis and characterizations of PrF_3 hollow nanoparticles," *Materials Letters*, vol. 61, no. 13, pp. 2765–2768, 2007.
- [20] I. Bilecka and M. Niederberger, "Microwave chemistry for inorganic nanomaterials synthesis," *Nanoscale*, vol. 2, no. 8, pp. 1358–1374, 2010.
- [21] C. Mi, Z. Tian, B. Han, C. Mao, and S. Xu, "Microwave-assisted one-pot synthesis of water-soluble rare-earth doped fluoride luminescent nanoparticles with tunable colors," *Journal of Alloys and Compounds*, vol. 525, pp. 154–158, 2012.
- [22] H. Wang, J.-R. Zhang, and J.-J. Zhu, "A microwave assisted heating method for the rapid synthesis of sphalerite-type mercury sulfide nanocrystals with different sizes," *Journal of Crystal Growth*, vol. 233, no. 4, pp. 829–836, 2001.
- [23] X. Wang and Y. Li, "Fullerene-like rare-earth nanoparticles," *Angewandte Chemie, International Edition*, vol. 42, no. 30, pp. 3497–3500, 2003.
- [24] A. Khorsand Zak, W. H. Abd Majid, M. E. Abrishami, and R. Yousefi, "X-ray analysis of ZnO nanoparticles by Williamson–Hall and size–strain plot methods," *Solid State Sciences*, vol. 13, no. 1, pp. 251–256, 2011.
- [25] V. K. Rai, D. K. Rai, and S. B. Rai, " Pr^{3+} doped lithium tellurite glass as a temperature sensor," *Sensors and Actuators A*, vol. 128, no. 1, pp. 14–17, 2006.
- [26] M. Kaczkan, Z. Boruc, B. Fetlinski, S. Turczynski, and M. Malinowski, "Temperature dependence of $^3\text{P}_0$ Pr^{3+} fluorescence dynamics in $\text{Y}_4\text{Al}_2\text{O}_9$ crystals," *Applied Physics B: Lasers and Optics*, vol. 113, no. 2, pp. 277–283, 2013.
- [27] I. Kamma, P. Kommidi, and B. R. Reddy, "High temperature measurement using luminescence of Pr^{3+} doped YAG and Ho^{3+} doped CaF_2 ," *Physica Status Solidi (c)*, vol. 6, no. S1, pp. S187–S190, 2009.
- [28] G. Tessier, M. Bardoux, C. Boué, C. Filloy, and D. Fournier, "Back side thermal imaging of integrated circuits at high spatial resolution," *Applied Physics Letters*, vol. 90, no. 17, article 171112, 2007.
- [29] M. S. Pudovkin, S. L. Korableva, A. O. Krashenninnicova et al., "Toxicity of laser irradiated photoactive fluoride PrF_3 nanoparticles toward bacteria," *Journal of Physics: Conference Series*, vol. 560, article 012011, 2014.
- [30] E. M. Alakshin, D. S. Blokhin, A. M. Sabitova et al., "Experimental proof of the existence of water clusters in fullerene-like PrF_3 nanoparticles," *JETP Letters*, vol. 96, no. 3, pp. 181–183, 2012.
- [31] G. Cao and Y. Wang, *Nanostructures and Nanomaterials. Synthesis, Properties, and Application*, World Scientific, 2nd edition, 2011.
- [32] L. Bao, Z. Li, Q. Tao, J. Xie, Y. Mei, and Y. Xiong, "Controlled synthesis of uniform LaF_3 polyhedrons, nanorods and nanoplates using NaOH and ligands," *Nanotechnology*, vol. 24, no. 14, pp. 145604–145609, 2013.
- [33] K. A. Aly, N. M. Khalil, Y. Algamal, and Q. M. A. Saleem, "Estimation of lattice strain for zirconia nano-particles based on Williamson–Hall analysis," *Materials Chemistry and Physics*, vol. 193, pp. 182–188, 2017.
- [34] R. Sivakami, S. Dhanuskodi, and R. Karvembu, "Estimation of lattice strain in nanocrystalline RuO_2 by Williamson–Hall and size–strain plot methods," *Spectrochimica Acta Part A: Molecular and Biomolecular Spectroscopy*, vol. 152, pp. 43–50, 2016.
- [35] P. P. Fedorov, M. N. Mayakova, S. V. Kuznetsov et al., "Phase diagram of the NaF – CaF_2 system and the electrical conductivity of a CaF_2 -based solid solution," *Russian Journal of Inorganic Chemistry*, vol. 61, no. 11, pp. 1472–1478, 2016.
- [36] P. P. Fedorov, M. N. Mayakova, V. A. Maslov et al., "The solubility of sodium and potassium fluorides in strontium fluoride," *Nanosystems: Physics, Chemistry, Mathematics*, vol. 8, no. 6, pp. 830–834, 2017.
- [37] A. Mech, M. Karbowiak, L. Kepinski, A. Bednarkiewicz, and W. Strek, "Structural and luminescent properties of nano-sized NaGdF_4 : Eu^{3+} synthesised by wet-chemistry route," *Journal of Alloys and Compounds*, vol. 380, no. 1–2, pp. 315–320, 2004.
- [38] T. Grzyb and S. Lis, "Photoluminescent properties of LaF_3 : Eu^{3+} and GdF_3 : Eu^{3+} nanoparticles prepared by co-precipitation method," *Journal of Rare Earths*, vol. 27, no. 4, pp. 588–592, 2009.
- [39] Z. Wang, C. Liu, Y. Wang, and Z. Li, "Solvent-assisted selective synthesis of NaLaF_4 and LaF_3 fluorescent nanocrystals via a facile solvothermal approach," *Journal of Alloys and Compounds*, vol. 509, no. 5, pp. 1964–1968, 2011.
- [40] L. Nie, Y. Shen, X. Zhang et al., "Selective synthesis of LaF_3 and NaLaF_4 nanocrystals via lanthanide ion doping," *Journal of Materials Chemistry C*, vol. 5, no. 35, pp. 9188–9193, 2017.

- [41] J. Ladol, H. Khajuria, S. Khajuria, and H. N. Sheikh, "Hydrothermal synthesis, characterization and luminescent properties of lanthanide-doped NaLaF_4 nanoparticles," *Bulletin of Materials Science*, vol. 39, no. 4, pp. 943–952, 2016.
- [42] A. Sarakovskis, J. Grube, A. Mishnev, and M. Springis, "Up-conversion processes in $\text{NaLaF}_4\text{:Er}^{3+}$," *Optical Materials*, vol. 31, no. 10, pp. 1517–1524, 2009.
- [43] L. Rao, W. Lu, G. Ren et al., "Monodispersed LaF_3 nanocrystals: shape-controllable synthesis, excitation-power-dependent multi-color tuning and intense near-infrared upconversion emission," *Nanotechnology*, vol. 25, article 065703, pp. 1–8, 2014.
- [44] P. Scherrer, "Bestimmung der Größe und der inneren Struktur von Kolloidteilchen mittels Röntgenstrahlen," *Nachrichten von der Gesellschaft der Wissenschaften zu Göttingen, Mathematisch-Physikalische Klasse*, vol. 26, pp. 98–100, 1918.
- [45] J. I. Langford and A. J. C. Wilson, "Scherrer after sixty years: a survey and some new results in the determination of crystallite size," *Journal of Applied Crystallography*, vol. 11, no. 2, pp. 102–113, 1978.
- [46] A. R. Stokes and A. J. C. Wilson, "The diffraction of X rays by distorted crystal aggregates - I," *Proceedings of the Physical Society*, vol. 56, no. 3, pp. 174–181, 1944.
- [47] S. G. Pandya, J. P. Corbett, W. M. Jadwisieniczak, and M. E. Kordes, "Structural characterization and X-ray analysis by Williamson–Hall method for erbium doped aluminum nitride nanoparticles, synthesized using inert gas condensation technique," *Physica E: Low-dimensional Systems and Nanostructures*, vol. 79, pp. 98–102, 2016.
- [48] E. M. Alakshin, A. M. Gazizulina, R. R. Gazizulin et al., "The spin kinetics of ^3He in contact with nanosized crystalline powders LaF_3 ," *Journal of Physics: Conference Series*, vol. 568, no. 1, article 012001, 2014.
- [49] H. Okamoto, K. Kasuga, I. Hara, and Y. Kubota, "Visible–NIR tunable Pr^{3+} -doped fiber laser pumped by a GaN laser diode," *Optics Express*, vol. 17, no. 22, article 20227, 20232 pages, 2009.
- [50] J. W. Stouwdam, G. A. Hebbink, J. Huskens, and F. C. J. M. van Veggel, "Lanthanide-doped nanoparticles with excellent luminescent properties in organic media," *Chemistry of Materials*, vol. 15, no. 24, pp. 4604–4616, 2003.
- [51] J. W. Stouwdam and F. C. J. M. van Veggel, "Near-infrared emission of redispersible Er^{3+} , Nd^{3+} , and Ho^{3+} doped LaF_3 nanoparticles," *Nano Letters*, vol. 2, no. 7, pp. 733–737, 2002.
- [52] K. Ramasesha, L. D. Marco, A. Mandal, and A. Tokmakoff, "Water vibrations have strongly mixed intra- and intermolecular character," *Nature Chemistry*, vol. 5, no. 11, pp. 935–940, 2013.
- [53] P. M. Selzer, D. S. Hamilton, R. Flach, and W. M. Yen, "Phonon-assisted energy migration in $\text{Pr}^{3+}\text{:LaF}_3$," *Journal of Luminescence*, vol. 12–13, pp. 737–741, 1976.
- [54] K. K. Pukhov, Y. V. Orlovskii, and T. T. Basiev, "Spontaneous and stimulated transitions in impurity dielectric nanoparticles," in *Recent Optical and Photonic Technologies*, K. Y. Kim, Ed., p. 450, INTECH, Croatia, 2010, downloaded from SCIYO.COM.
- [55] A. Vanetsev, K. Kaldvee, L. Puust et al., "Relation of crystallinity and fluorescent properties of $\text{LaF}_3\text{:Nd}^{3+}$ nanoparticles synthesized with different water-based techniques," *Chemistry Select*, vol. 2, pp. 4874–4881, 2017.
- [56] M. S. Pudovkin, A. Morozov, V. V. Pavlov et al., "Physical background for luminescence thermometry sensors based on $\text{Pr}^{3+}\text{:LaF}_3$ crystalline particles," *Journal of Nanomaterials*, vol. 2017, Article ID 3108586, 9 pages, 2017.
- [57] V. V. Semashko, M. S. Pudovkin, A.-C. Cefalas et al., "Tiny rare-earth fluoride nanoparticles activate tumour cell growth via electrical polar interactions," *Nanoscale Research Letters*, vol. 13, no. 1, p. 370, 2018.
- [58] S. Sivakumar, P. R. Diamante, and F. C. J. M. van Veggel, "Silica-coated Ln^{3+} doped LaF_3 nanoparticles as robust down- and upconverting biolabels," *Chemistry - A European Journal*, vol. 12, no. 22, pp. 5878–5884, 2006.

